

A phase-field approach to conchoidal fracture

Carola Bilgen · Alena Kopaničáková · Rolf Krause · Kerstin Weinberg

Received: 4 April 2017 / Accepted: 8 August 2017 / Published online: 28 August 2017
© Springer Science+Business Media B.V. 2017

Abstract Crack propagation involves the creation of new internal surfaces of a priori unknown paths. A first challenge for modeling and simulation of crack propagation is to identify the location of the crack initiation accurately, a second challenge is to follow the crack paths accurately. Phase-field models address both challenges in an elegant way, as they are able to represent arbitrary crack paths by means of a damage parameter. Moreover, they allow for the representation of complex crack patterns without changing the computational mesh via the damage parameter—which however comes at the cost of larger spatial systems to be solved. Phase-field methods have already been proven to predict complex fracture patterns in two and three dimensional numerical simulations for brittle fracture. In this paper, we consider phase-field models and their numerical simulation for conchoidal fracture. The main characteristic of conchoidal fracture is that the point of crack initiation is typically located inside of the body. We

present phase-field approaches for conchoidal fracture for both, the linear-elastic case as well as the case of finite deformations. We moreover present and discuss efficient methods for the numerical simulation of the arising large scale non-linear systems. Here, we propose to use multigrid methods as solution technique, which leads to a solution method of optimal complexity. We demonstrate the accuracy and the robustness of our approach for two and three dimensional examples related to mussel shell like shape and faceted surfaces of fracture and show that our approach can accurately capture the specific details of cracked surfaces, such as the rippled breakages of conchoidal fracture. Moreover, we show that using our approach the arising systems can also be solved efficiently in parallel with excellent scaling behavior.

Keywords Phase field · Multigrid method · Brittle fracture · Crack initiation · Conchoidal fracture

C. Bilgen · K. Weinberg (✉)
Lehrstuhl für Festkörpermechanik, Department
Maschinenbau, Universität Siegen, Paul-Bonatz-Straße
9-11, 57068 Siegen, Germany
e-mail: kerstin.weinberg@uni-siegen.de

A. Kopaničáková · R. Krause
Chair for Advanced Scientific Computing, Institute of
Computational Science, USI - Università della Svizzera
italiana, Via Giuseppe Buffi 13, 6900 Lugano,
Switzerland

1 Introduction

The prediction of crack nucleation and fragmentation pattern is one of the main challenges in solid mechanics. Every crack in a solid forms a new surface of an a priori unknown position which needs to be identified. In order to compute such moving boundary problems, phase-field approaches have recently gained attention, see, e.g., [6, 10, 17, 21, 24, 36].

The main idea behind this approach is to mark the material's state by an order parameter field $z(\mathbf{x}, t)$, and to let it evolve in space and time. The order parameter—or phase—field is by definition a continuous field and thus, the moving crack boundaries are 'smeared' over a small but finite length. Therefore, phase field models constitute so-called diffuse-interface formulations. This raises the question of how detailed the method can capture the specific details of cracked surfaces, like, e.g., the bend and rippled breakages of conchoidal fracture.

Conchoidal fracture is a specific type of brittle fracture which is observed in fine-grained or amorphous materials such as rocks, minerals and glasses. The solid material breaks by cleavage but does not follow any natural planes of separation. In contrast to the faceted fractures often seen in crystalline materials, conchoidal fracture typically results in a curved breakage, see Fig. 1, that resembles the rippling, gradual curves of a sea shell, so called Wallner lines [37]—which gives the name “conchoid” (like a conch or shell). Since in conchoidal fracture the shape of the broken surface is controlled only by the stresses state, and not by some preferred orientation of the material, it provides a record of the stress state at the time of failure. The point of crack initiation is typically located inside the body and not on the structure's surface. Therefore, it will serve us here as a benchmark to test the ability of the phase-field approach to predict crack nucleation and fracture in a brittle material, without any notch, kerf, flaw or initial crack.

In the remaining paper we will proceed as follows: In the next section we present the basic equations of the phase-field approach to fracture for both, linear-elastic fracture and finite deformations. In Sect. 3 the temporal and spatial discretization is provided. A particular solution technique based on a multigrid

method is formulated in Sect. 4. In Sect. 5 we present a two-dimensional numerical example for the simple but typical problem of an elastic bloc pulled on a part of its boundary. This problem is related to the Hertzian contact of a rigid punch on a half-space and therefore, an analytical solution of the stress-state at crack initiation is known. We will use this as a reference to evaluate the numerical solution for varying model parameters. Finally, in Sect. 6 we analyze the three-dimensional problem of conchoidal fracture below the surface of a pulled stone block and in Sect. 7 we add a study on the performance of our multigrid solver in this benchmark problem. Our results show, that a phase-field approach to fracture is able to capture the essential features of conchoidal fracture in both, the linearized and the finite deformation regime.

2 Phase-field approach

Let us consider a solid with domain $\Omega \subset \mathbb{R}^3$ and boundary $\partial\Omega \equiv \Gamma \subset \mathbb{R}^2$ deforming within a time interval $t \in [0, t_{\text{tot}}] \subset \mathbb{R}^+$. Crack growth corresponds to the creation of new boundary surfaces $\Gamma(t)$. Hence the total potential energy of a homogenous but cracking solid is composed of its material's energy with free Helmholtz energy density Ψ^{mat} and of surface energy contributions from growing crack boundaries.

$$E = \int_{\Omega} \Psi^{\text{mat}} d\Omega + \int_{\Gamma(t)} \mathcal{G}_c d\Gamma \quad (1)$$

The fracture-energy density \mathcal{G}_c quantifies the material's resistance to cracking, for brittle fracture it corresponds to Griffith's critical energy release rate. However, the energy functional (1) cannot be optimized in general and even an incremental approach is challenging because of the moving boundaries $\Gamma(t)$. Sophisticated discretization techniques have been developed to solve such problems, e.g. cohesive zone models [28, 30, 40], the extended finite element method [23, 35], eroded finite elements or recently developed eigenfracture strategies [29, 33].

In a phase-field approach to fracture, the additional field $z(\mathbf{x}, t)$ with $z \in [0, 1]$ characterizes the state of the material, whereby $z = 0$ indicates the solid and $z = 1$ the broken state. The set of evolving crack boundaries

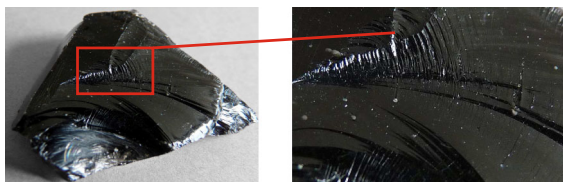


Fig. 1 The typical curved breakages and conch-like surfaces of conchoidal fracture can nicely be observed in fragments of volcanic glass *Source* of the original photo is [1]

is now replaced by a surface-density function $\gamma = \gamma(z(\mathbf{x}, t))$ and an approximation of the form

$$\int_{\Gamma(t)} d\Gamma \approx \int_{\Omega} \gamma(z(\mathbf{x}, t)) d\Omega \quad (2)$$

which allows to re-write the total potential energy of a cracking solid and to formulate the optimization problem locally.

$$E = \int_{\Omega} (\Psi^{\text{mat}} + \mathcal{G}_c \gamma) d\Omega \rightarrow \text{optimum} \quad (3)$$

In potential (3) the material's energy is composed of two terms, a bulk energy density Ψ^{mat} and a surface energy contribution $\mathcal{G}_c \gamma$. By definition γ is only different from zero along cracks.

There is no unique way to choose the crack density function; a typical form is the the second-order phase-field approach:

$$\gamma(z, \nabla z) = \frac{1}{2l_c} z^2 + \frac{l_c}{2} |\nabla z|^2 \quad (4)$$

At a crack, the first term in Eq. (4) describes a jump and the gradient regularizes the discontinuity; the length-scale parameter l_c weights the influence of the gradient term. Inserted into functional (3) it forms a potential which corresponds to the well known Ambrosio-Tortorelli functional of continuum damage mechanics [3]. Thus, the phase-field fracture approach can be seen as a gradient damage model with the major difference, that the order parameter z indicates the material to be either intact ($z = 0$) or broken ($z = 1$), intermediated states are not physically meaningful. The length l_c in (4) is a measure for the width of the diffuse transition zone, see Fig. 2, and additional high

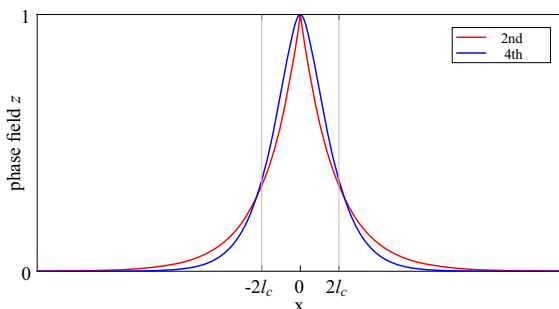


Fig. 2 Uniaxial model with a crack at $x = 0$ and with a continuous phase field $z \in [0, 1]$; phase field approximation for a second order and a fourth order approximation of crack density function γ

order terms may improve the crack approximation properties of function (4), cf. [7, 39].

The evolution of the phase-field is stated here in a general form

$$\dot{z} = MY, \quad (5)$$

where parameter M describes a kinematic mobility and $Y = Y(z, \dots)$ summarizes all driving forces which typically represent a competition of bulk material and surface forces.

In consequence, the specific phase-field model is characterized by the crack-density function (4) and, furthermore, by the components of the free energy which form the driving force for crack growth. Specifically, we consider brittle fracture here and so the material's strain Helmholtz free energy density is purely elastic, $\Psi^{\text{mat}} = \Psi^e$. In the following a linear and a nonlinear material model are proposed und their split into compressive and tensile components—which are responsible for crack growth—is described. The governing balance equations for the phase-field fracture are summarized in Table 1.

2.1 Linear-elastic fracture mechanics

In classical linear elasticity with displacement field $\mathbf{u}(\mathbf{x}, t) : \Omega \times [0, t_{\text{tot}}] \rightarrow \mathbb{R}^3$, the strain energy function is defined as

$$\Psi^e(\varepsilon) = \frac{1}{2} \varepsilon(\mathbf{u}) : \mathbb{C}^\star(z) : \varepsilon(\mathbf{u}), \quad (6)$$

where $\varepsilon(\mathbf{u}) = \text{sym}(\nabla \mathbf{u})$ is the strain tensor; \mathbb{C} is the Hookean material tensor, and $\mathbb{C}^\star(z)$ denotes an adapted or degraded material tensor of the form

$$\mathbb{C}^\star(z) = g(z)\mathbb{C} \quad \text{with} \quad g(z) = (1 - z)^2 + z_e. \quad (7)$$

Table 1 Balance equations for a cracking solid subjected to body forces $\bar{\mathbf{b}}$ in Ω , prescribed displacements $\bar{\mathbf{u}}$ on $\partial\Omega_1$ and tractions $\bar{\mathbf{t}}$ on $\partial\Omega_2$ with $\partial\Omega_1 \cup \partial\Omega_2 = \partial\Omega$

Balance of linear momentum	$\text{div}(\sigma) + \bar{\mathbf{b}} = \rho_0 \ddot{\mathbf{u}} \quad \text{on } \Omega$
Boundary conditions	$\mathbf{u} = \bar{\mathbf{u}} \quad \text{on } \partial\Omega_1$
	$\sigma \cdot \mathbf{n} = \bar{\mathbf{t}} \quad \text{on } \partial\Omega_2$
Phase-field equation	$z - 4l_c^2 \Delta z = 1 \quad \text{on } \Omega$
Boundary conditions	$z = 0 \quad \text{on } \partial\Omega_1$
	$\nabla z \cdot \mathbf{n} = 0 \quad \text{on } \partial\Omega_2$

Function $g(z)$ is a degradation function; it accounts for the loss of stiffness in the crack. The specific form of $g(z)$ is open to modeling, as long as the conditions

$$g(0) = 1, \quad g(1) = 0, \quad g'(1) = 0 \quad (8)$$

are fulfilled. We choose here the simplest degradation function $g(z) = (1 - z)^2$, and refer to [38] for further discussion. However, for the use in material model (7) it is common to add a small parameter z_ε for numerical reasons.

The compression-tension anisotropy of fracture, i.e., the fact, that only tensile stress states contribute to the crack propagation, makes an appropriate decomposition of the elastic strain-energy necessary. The energy (6) needs to be split into a tensile and a compressive part whereby only the first is influenced by the phase-field parameter:

$$\Psi^e(\varepsilon, z) = g(z)\Psi^{e+} + \Psi^{e-} \quad (9)$$

with $\Psi^{e\pm} = \frac{1}{2}\varepsilon^\pm(\mathbf{u}) : \mathbb{C} : \varepsilon^\pm(\mathbf{u})$ and $\varepsilon^\pm(\mathbf{u})$ being the positive and the negative part strain tensor. We base this split on the spectral decomposition of the strain tensor

$$\varepsilon = \sum_{a=1}^3 \varepsilon_a \mathbf{n}_a \otimes \mathbf{n}_a,$$

where ε_a denote the principal strains and \mathbf{n}_a the corresponding principal directions, $a = 1, 2, 3$. Based on this representations and using the Macaulay brackets to describe the ramp functions of the positive/negative part,

$$\langle x \rangle^+ = \frac{1}{2}(x + |x|) \quad \langle x \rangle^- = \frac{1}{2}(x - |x|) \quad (10)$$

we define the positive and the negative parts of the strain tensor as

$$\varepsilon^\pm = \sum_{a=1}^3 \langle \varepsilon_a \rangle^\pm \mathbf{n}_a \otimes \mathbf{n}_a.$$

The positive parts contain contributions due to positive dilatation and contributions due to positive principal strains, and only this part of the strain energy is responsible for crack growth. A similar decomposition can be deduced for the stress tensor σ . This decomposition guarantees not only that tension within

a crack cannot contribute to the energy of the body but gives also a physically meaningful positive crack driving force.

2.2 Fracture in finite elasticity

The general concept of Griffith's critical energy release rate and the corresponding potential energy (3) is limited to brittle fracture but does not presume small deformations. The approach is also valid in the finite deformation regime with deformation mapping $\chi(\mathbf{x}, t) : \Omega \times [0, t_{\text{tot}}] \rightarrow \mathbb{R}^3$. We define the deformation gradient

$$\mathbf{F} = \nabla_{\mathbf{x}} \chi = \frac{\partial \chi}{\partial \mathbf{X}} \quad (11)$$

where the fields in capitals refer to the initial configuration; work conjugate is the first Piola-Kirchhoff stress tensor.

$$\mathbf{P} = \frac{\partial \Psi^e}{\partial \mathbf{F}} \quad (12)$$

The second Piola-Kirchhoff stress tensor $\mathbf{S} = \mathbf{F}^{-1}\mathbf{P}$ and the Cauchy stresses are calculated via the usual relations, $\sigma = J^{-1}\mathbf{F}\mathbf{S}\mathbf{F}^T$ and analogously to (7) they depend on phase-field z . Here and in the following we write $J = \det F$.

For the application we have in mind we expect non-linear behavior but not 'rubbery' deformations and, therefore, we restrict ourselves to Neo-Hookean type of materials extended to the volumetric range, cf. [8, 38]. With the incompressible first invariant of the right and left Cauchy-Green deformation tensor $I_C = J^{-1/3}\mathbf{F} : \mathbf{F}$ and Lamé constants μ and λ the corresponding strain energy density reads

$$\Psi^e = \frac{\kappa}{2}(J - 1)^2 + \frac{\mu}{2}(I_C - 3). \quad (13)$$

The elastic strain energy density (13) has to account for the compression-tension anisotropy of fracture, i.e., it needs to be reduced to a tensile component Ψ^{e+} which drives a crack to grow. Moreover, for the existence of a minimum and stable numerical approximation Ψ^e needs to be polyconvex, a requirement which can be fulfilled by a decomposition of the invariants in tensile and compressive parts as follows [18].

$$I_C^\pm = 3 + J^{-2/3} \langle \mathbf{F} : \mathbf{F} - 3 \rangle^\pm, \quad (14)$$

$$J^\pm = 1 + \langle \det \mathbf{F} - 1 \rangle^\pm. \quad (15)$$

Exemplarily, the split of the first invariant is shown in Fig. 3. Then the positive and negative parts of the strain energy function follow as

$$\Psi^{e\pm}(\mathbf{F}, z) = \frac{\kappa}{2} (J^\pm - 1)^2 + \frac{\mu}{2} (I_C^\pm - 3). \quad (16)$$

In consequence, the energy (13) also decomposes into tension induced and compression induced components.

$$\Psi^e(\mathbf{F}, z) = g(z) \Psi^{e+} + \Psi^{e-} \quad (17)$$

2.3 Crack driving force and irreversibility

Minimization of the total potential energy of a cracking solid (1) or (3) requires the optimality condition $\dot{E} = 0$. This gives the local condition $\dot{\Psi}^e + \mathcal{G}_c \dot{\gamma} = 0$. Expressed with the total or variational derivative

$$\delta_z \bullet = \frac{\partial \bullet}{\partial z} - \nabla_{\mathbf{x}} \cdot \left(\frac{\partial \bullet}{\partial \nabla z} \right) \quad (18)$$

we write equivalently $\delta_z(\Psi^e + \mathcal{G}_c \gamma) \dot{z} = 0$. We define the expression

$$Y = \delta_z(\Psi^e + \mathcal{G}_c \gamma) \quad (19)$$

as the work conjugate driving force for the phase-field evolution.

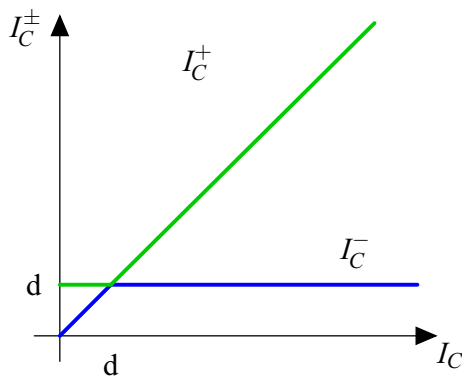


Fig. 3 Illustration of the anisotropic split of the first invariant into tensile and compressive parts with dimension $d \in \{2, 3\}$

Moreover, irreversibility of crack growth requires with representation (2)

$$\frac{d}{dt} \int_{\Omega} \mathcal{G}_c \gamma \, d\Omega = \int_{\Omega} \delta_z(\mathcal{G}_c \gamma) \dot{z} \, d\Omega \geq 0, \quad (20)$$

which gives irreversibility conditions for the phase-field evolution. Specifically, global irreversibility of crack growth leads to the conditions of a locally positive functional derivative of the crack density $\delta \gamma \geq 0$ and a positive evolution of the crack phase-field $\dot{z} \geq 0$. The first constraint follows naturally when the crack driving force accounts for the anisotropy of tension and compression, i.e. by a constitutive assumption that relates the functional derivative to a positive energetic driving force. The second constraint is a natural assumption for the non-reversible evolution of cracks.

In consequence, we obtain the evolution of the phase-field by a restriction of Eq. (5) to

$$\dot{z} = M \langle Y \rangle^+ \quad \text{in } \Omega_0 \times [0, t_{\text{tot}}] \quad (21)$$

which evolves for the second order approach (4) with $l_c \delta_z \gamma = z - l_c^2 \Delta z$ to

$$\dot{z} = M \langle \delta_z \Psi^e + \mathcal{G}_c (z - l_c^2 \Delta z) \rangle^+ \quad (22)$$

with boundary conditions

$$\nabla z \cdot \mathbf{n} = 0 \quad \text{on } \partial \Omega_0. \quad (23)$$

The initial conditions are given with $z(\mathbf{x}, 0) = 0$ on Ω_0 , describing an unbroken state.

A similar variational functional of brittle fracture was first introduced by Francfort and Marigo [12] and Bourdin [9] and with some modifications this ansatz has become very popular since, see, e.g., Kuhn and Müller [22], Miehe et al. [25] and Abdollahi and Arias [2], Borden et al. [6], and Hesch et al. [19].

3 Discretisation

3.1 Weak forms and discretization

The elastic boundary value problem follows from the balance of linear momentum and the crack phase-field evolution which is controlled by the corresponding elastic energy, cf. Table 1. Restated in the weak form, the coupled problem reads: Find $\mathbf{u} \in \mathcal{V}^u$ and $z \in \mathcal{V}^z$ such that

$$\begin{aligned}
& \int_{\Omega} \rho_0 \ddot{\mathbf{u}} \cdot \delta \mathbf{u} \, d\Omega + \int_{\Omega} \mathbf{P} : \nabla(\delta \mathbf{u}) \, d\Omega \\
&= \int_{\Omega} \bar{\mathbf{b}} \cdot \delta \mathbf{u} \, d\Omega + \int_{\Gamma_2} \bar{\mathbf{t}} \cdot \delta \mathbf{u} \, d\Gamma \quad \forall \delta \mathbf{u} \in \mathcal{V}_0^u,
\end{aligned} \quad (24)$$

and

$$\begin{aligned}
& \int_{\Omega} \dot{z} \cdot \delta z \, d\Omega + \int_{\Omega} \frac{\partial \Psi^e}{\partial z} \cdot \delta z \, d\Omega + 2\mathcal{G}_c l_c \int_{\Omega} \nabla z \nabla(\delta z) \, d\Omega \\
& - \frac{\mathcal{G}_c}{2l_c} \int_{\Omega} (1-z) \cdot \delta z \, d\Omega = 0 \quad \forall \delta z \in \mathcal{V}_0^z.
\end{aligned} \quad (25)$$

The functional space of admissible mechanical fields is $\mathcal{V}^u = \{\mathbf{u} \in \mathcal{H}^1(\Omega) \mid \forall t \in [0, t_{\text{tot}}]\}$, where \mathcal{H}^1 denotes the Sobolev functional space of square integrable functions with square integrable weak first derivatives. Index 0 denotes the additional constraint $\delta \mathbf{u} = \mathbf{0}$ on Γ_1 . Correspondingly the space of admissible phase-fields is $\mathcal{V}^z = \{z \in \mathcal{H}^1(\Omega) \mid \forall t \in [0, t_{\text{tot}}] \mid z \in [0, 1]\}$ and $\mathcal{V}_0^z = \{\delta z \in \mathcal{V}^z \mid \delta z = 0 \text{ on } \partial\Omega(t)\}$. In the linear material model the stresses σ coincide with \mathbf{P} in (24), we do not repeat the corresponding weak formulation here.

For finite element implementation the domain Ω is subdivided into a set of non-overlapping elements such that

$$\Omega \approx \Omega^h = \bigcup_{e=1}^{n_e} \Omega_e. \quad (26)$$

We make use of a classical ansatz and approximate the displacement field and its variation with

$$\mathbf{u} \approx \mathbf{u}^h = \sum_{i=1}^{n_k} N_i \hat{\mathbf{u}}^{(i)}, \quad \delta \mathbf{u}^h \approx \sum_{i=1}^{n_k} N_i \delta \hat{\mathbf{u}}^{(i)}, \quad (27)$$

where the shape function N_i are piecewise Lagrangian polynomials and $\hat{\mathbf{u}}^{(i)}$ contains all unknown nodal displacements \hat{u}_i of the n_k nodes. For the phase-field we approximate

$$z \approx z^h = \sum_{i=1}^{n_k} \tilde{N}_i \hat{z}^{(i)}, \quad \delta z^h = \sum_{i=1}^{n_k} \tilde{N}_i \delta \hat{z}^{(i)} \quad (28)$$

with ansatz functions $\tilde{N}_1, \dots, \tilde{N}_{n_k}$ and nodal values $\hat{z}^{(i)}$. In the following Sects. 5 and 6 we apply the same ansatzfunctions for the displacement field and the phase-field.

For the time integration we divide the considered time interval $[0, t_{\text{tot}}]$ into n_t pairwise disjoint equidistant subintervals $I_n = [t_n, t_{n+1}]$ with time step $\Delta t := t_{n+1} - t_n$ and employ an implicit Crank–Nicolson scheme, known to be second-order accurate. Plugging (27) and (28) into (24, 25) gives after a straightforward calculation the finite element system of equations.

3.2 Solution strategies

Two popular solution strategies for solving the non-linear discrete systems arising from (24)–(25) in each time-step are monolithic [25] and staggered [24] schemes. Whereas the monolithic approach the fully-coupled non-linear system is solved in each loading step/time-step and works only applying a viscous term or a modification to the stiffness matrix, see [15], in the staggered approach the evolution operator is split algorithmically into the phase field z and the displacement field \mathbf{u} . Then, in each time step we successively solve for both quantities. Numerical evidence shows that in general the staggered approach is more robust than the monolithic one, but that it tends to underestimate the speed of the crack evolution, as the spatial systems are solved only approximately. We note that therefore, only small loading steps can be applied. Due to this reason, we combine the staggered scheme with an adaptive time-stepping strategy, as proposed in [24]. Furthermore, within the staggered scheme sub-iterations can be applied to approximate the final equilibrium solution more precisely, as can be seen from Algorithm 1.

Algorithm 1 Staggered solution scheme

```

1: for  $t = 0, \dots, t_{\text{tot}}$  do
2:   while  $\|\mathbf{u}_{t+1} - \mathbf{u}_t\| > \varepsilon$  &&  $\|z_{t+1} - z_t\| > \varepsilon$  do
3:     Compute fracture phase field:
4:      $z_{t+1} = \arg \inf_{z_t} \{ \int_{\Omega} \mathcal{G}_c[\gamma(z_t, \nabla z_t) - ((1 - z_t)^2 + z_\varepsilon) \psi_t^{e+}] d\Omega \}$ 

5:     Compute displacement field:
6:      $\mathbf{u}_{t+1} = \arg \inf_{\mathbf{u}_t} \{ \int_{\Omega} \psi^e(\mathbf{P}_t, z_{t+1}) \mathbf{u}_t - \mathbf{b} \mathbf{u}_t d\Omega - \int_{\partial\Omega^\sigma} \bar{\mathbf{t}} \mathbf{u}_t d\partial\Omega^\sigma \}$ 
7:   end while
8: end for

```

3.2.1 Subproblems

By design, the staggered scheme gives rise to two separate minimization problems, see Algorithm 1. In the phase field subproblem, we look for phase field z , by minimizing the quadratic function which is resulting from fixing the displacement \mathbf{u} . In the second step we solve for the displacement field u by minimizing the elastic energy for the fixed phase field z obtained in the first sub-step. We note that the latter does not necessarily give rise to a convex quadratic minimization problem. For example, in case of a linear elastic material with infinitesimal strain we will be lead to a convex quadratic functional, whereas in the more general case case of a non-linear material with finite strain theory we have to deal with a nonlinear and poly-convex elastic energy.

A standard approach for dealing with the resulting non-linearity in the necessary first-order conditions for a minimizer is Newton's method, as it is simple and locally quadratical convergent. A single Newton iteration is defined by

$$\delta \mathbf{u}_{k+1} = \delta \mathbf{u}_k - \alpha \mathbf{J}^{-1} \mathbf{R}. \quad (29)$$

Here, the iteration number is denoted by subscript k , $\alpha \in \mathbf{R}^+$ is a damping or step-size parameter and the matrix $\mathbf{J} \in \mathbb{R}^{n \times n}$ represents the Jacobian, i.e the tangent stiffness matrix.

3.2.2 Linear solvers

The first order necessary conditions for solving the unconstrained quadratic minimization problem gives directly rise to a linear system of equations. For the solution of the non-linear mechanical subproblem, we employ Newton's method as stated earlier above,

which leads to a linear system to be solved in each of the Newton steps.

Solving these systems can become computationally highly demanding due to the fact that in order to resolve the regularized crack surface Γ_l , a fine mesh with a high spatial resolution is required.

In fact, for resolving the smoothed crack sufficiently accurate, the mesh size h has to fulfill

$$h < \frac{l_c}{2}, \quad (30)$$

see [25]. Here, l_c is the length-scale parameter from (4) for the width of the diffusive crack zone. We note that in general adaptive refinement strategies are not guaranteed to significantly reduce the computational burden, as the crack path is hard to predict and correspondingly the mesh for the damage parameter has to be chosen sufficiently fine on the whole computational domain. As a consequence, we end up with large-scale non-linear systems. These systems might also be ill-conditioned, since the growing crack will lead to strongly spatially varying stiffness parameters.

Here, we employ multigrid methods in combination with Krylov-space methods for the solution of the linear systems for the phase field z and for the displacements u . In contrast to direct methods such as LU or Cholesky factorization [14], multigrid is of optimal complexity and thus more efficient for large scale systems, in terms of floating point operations as well as in terms of memory requirements. A comparison of time complexity for different linear solvers is depicted in Fig. 4. We note, however, that for smaller linear systems direct solvers can be extremely efficient. For example, modern sparse direct solvers, e. g. MUMPS [4], PARDISO [32] minimize both storage

and amount of required floating points by exploiting the structure of the matrices. These solvers exploit the good sparsity pattern very well and determine a pivot sequence, which leads to efficient factorization of the arising sparse systems. The factorization of systems with n unknowns as arising from Algorithm 1 requires $\mathcal{O}(n^2)$ flops in 3 spatial dimensions and $\mathcal{O}(n^{3/2})$ flops in 2 spatial dimensions. Nonetheless, when n becomes too large, direct solvers suffer from the quadratic growth of computational cost and memory. In contrast, multigrid requires $\mathcal{O}(n)$ flops in both cases and is also optimal in terms of memory usage. Moreover, multigrid can be parallelized easier and shows significantly better parallel scalability.

We use the multigrid method as a preconditioner within a Krylov-space method [31], such as GMRES or cg, in order to speed up the convergence. These methods require low computational cost and are well suited massively parallel environments, as their building blocks e.g. matrix-vector multiplication, dot product allow for hybrid parallelization.

4 Multigrid methods for phase field and fracture

Multigrid methods, see, e.g. [11], rely on a hierarchy $V_l, l = 1, \dots, L$ of usually nested finite element spaces. Here, we use subscript $l = 0, \dots, L-1$ in order to denote level and assume $L \geq 1$ to be the finest level. This hierarchy is constructed in the case of geometric multigrid methods based on a given (geometric)

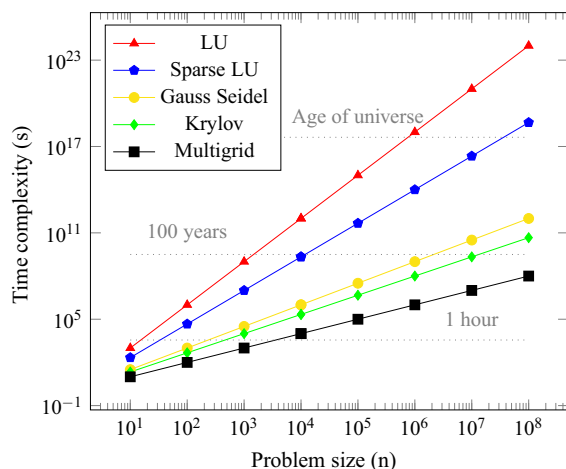


Fig. 4 Comparison of time complexity for different linear solvers

hierarchy of nested meshes $(\mathcal{T}_l)_{0 \leq l \leq L}$ with mesh-size h_l and a shape regular finite element triangulation \mathcal{T} of the domain Ω . We note that if no such mesh-hierarchy is given, the construction of the spaces $V_l, l = 1, \dots, L-1$ turns out to be a non-trivial task. Different approaches exist, including mesh-based coarsening strategies, auxiliary space methods, and Algebraic Multigrid Methods. In terms of memory usage and convergence speed, often geometric multigrid methods turn out to be the best choice.

In the context of the phase-field fracture models considered here, we are employing geometric multigrid methods. The mesh hierarchy is created by successively refining a given coarse mesh.

The eventual solution process combines two components: so called smoothing and coarse grid correction. The smoother, for example a simple iterative solver such as Gauss-Seidel [31] or Jacobi method, reduces the respective high frequency errors on each of the level. This corresponds to a multilevel decomposition of the error into different frequency ranges, each of which is dealt with on a different mesh by the smoother. The remaining low frequency error is removed by a direct solver on the coarsest level. This is traditionally done by means of a direct solver, e.g. LU factorization [14]. Since the size of the linear systems decreases by a factor of 8 in three spatial dimensions in the case of uniformly refined meshes $(\mathcal{T}_l)_{0 \leq l \leq L}$, the coarse level stiffness matrix can be assumed to be sufficiently small in size.

The transfer between subsequent spaces is done by means of prolongation/restriction operators. Whereas the prolongation operator \mathbf{P}_{l-1}^l maps coarse-grid

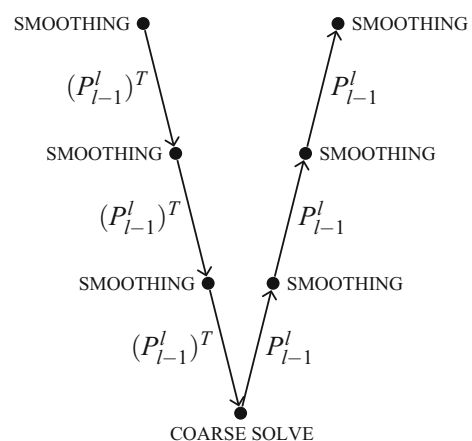


Fig. 5 Multigrid V-cycle

correction to the next finer level, the restriction operator, often chosen as $(\mathbf{P}_{l-1}^l)^T$, transfers the fine level residual to the coarse level, see Fig. 5.

Algorithm 2 depicts the recursive structure of a multigrid solver. The parameters $v_1, v_2 \geq 0$ denote the number of pre-smoothing and post-smoothing steps. The parameter $\gamma \geq 1$ indicates the amount of recursive calls of the coarse level correction routine.

The coarse level operators $(\mathbf{A}_l)_{l=0,\dots,L-1}$ used on the coarse levels V_l are obtained recursively via Galerkin-assembly, i.e.

$$\mathbf{A}_{l-1} = (\mathbf{P}_{l-1}^l)^T \mathbf{A}_l (\mathbf{P}_{l-1}^l) \quad l = L-1, \dots, 1. \quad (31)$$

As a consequence, the coarse level operators are assembled using information stemming from quadrature on the finest level L . This is of major importance, because the phase-field models employ the length-scale parameter l_c , which is tightly coupled to the mesh size h by means of relation (30).

$y \approx -0.5a$, see Fig. 7. The exact position depends on the poisson ration ν and on the size of the domain which is assumed to be infinite in the analytical solution. The other stress components decay monotonously. This suggests, that after pulling a rigid plate from the half space the maximum elastic strain energy density and thus a crack will appear at about $y = \frac{1}{2}a$.

For our phase-field fracture simulation a half space of 2×1 m is considered. The material data for the model are $\lambda = \mu = 20,000$ N/mm² which corresponds to $E = 50$ GPa and to a poisson number of 0.25. The critical energy release rate is $\mathcal{G}_c = 1$ N/mm. At the lower side the displacements are constrained in horizontal and vertical direction, respectively. The loaded upper boundary has the length $2a = 1$ m. At first we use a finite element mesh of 256×256 isoparametric eight-node elements which results in an element size of $h = 8$ mm. Geometry and deformation in z -direction are constant and so we assume a plane strain state. The computation is performed in a monotonic displacement-driven

Algorithm 2 $x_L = \text{MG}(A_L, x_L, f_L, v_1, v_2, \gamma)$

```

1:  $x_L := \text{smooth}^{v_1}(A_L, x_L, f_L)$ 
2:  $r_L = f_L - A_L u_L$ 
3:  $r_l = P_L^l r_L$ 
4: if  $l == 0$  then
5:    $c = A_l^{-1} r_l$ 
6: else
7:    $c = \text{MG}(A_l, 0, r_l, v_1, v_2, \gamma)$ 
8: end if
9:  $x_L := x_L + P_l^l c$ 
10:  $x_L := \text{smooth}^{v_2}(A_L, x_L, f_L)$ 
11: return  $x_L$ 

```

5 Fracture in an elastic half-space

As a first numerical example we chose a two-dimensional approximation of an infinite elastic half-space pulled at a part of its boundary with a prescribed vertical displacement $\mathbf{u}_z(x, 0) = \bar{u}$ for $-a \leq x \leq a$ with $a \in [0, l_x] \subset \mathbb{R}^+$. The remaining boundary of the half space is free. The problem is depicted in Fig. 6 and states basically a rigid punch problem. The nominal stress has singularities at the corners, $\sigma_y(\pm a, 0) \rightarrow \infty$.

In particular we know, that a pulled plate with with $2a$ induces a shear stress distribution which has its maximum in the symmetry axis of the problem at

setup, i.e. pulled at the upper boundary with $-a \leq x \leq a$. The prescribed displacement is applied incrementally until the half-space is fully cracked.

This example remains in a small strain state in all loadings. Fig. 9 shows the cracked surface in the half-space at the final state. The crack initiation starts at a position of $y = 0.7383$ m below the loaded boundary which corresponds to the expected location, see Fig. 8.

At next we vary the critical length parameter l_c of the phase field by $l_c \in \{0.02, 0.05, 0.1, 0.2\}$ m. Load–deflection curves in Fig. 10 show the typical interdependence between mesh size, the chosen length scale and the obtained results. Please note, that the effect of the length-scale parameter l_c is two-fold. On

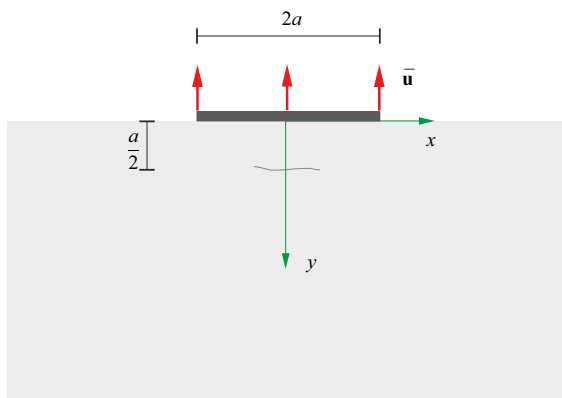


Fig. 6 Elastic half space pulled at part of its boundary $-a \leq x \leq a$ with a given displacement \bar{u} of a fixed rigid plate. The expected position of crack initiation is deduced from the analytical solution of as about $0.5a$

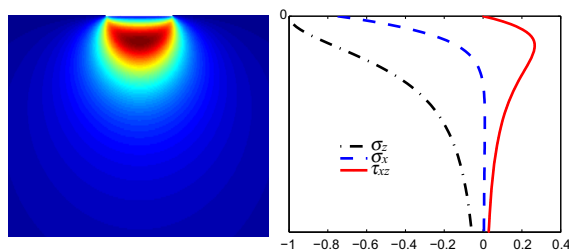


Fig. 7 Maximal shear stress distribution (*left*) and stress components along the symmetry axis in a half space punched by a rigid indenter

one hand, l_c is determined by the mesh size h because it has to be large enough to enable the approximation of a diffuse interface. This clearly shows a mesh dependence of the form $l_c > 2 \dots 3h$. On the other hand, l_c enters the material. In the sense of the Griffith criterium for crack growth the fracture energy, which is proportional to \mathcal{G}_c/l_c , competes with the elastic energy density Ψ^{e+} . Here l_c has the effect of a material parameter. This can be seen nicely in the load deflection curves of Fig. 10. All curves grow monotonously up to a maximum load at about $\bar{u} = 7.5$ mm prescribed displacement. However, the maximum load value rises with decaying length l_c . Only a constant ratio \mathcal{G}_c/l_c together the same width of the diffuse crack zone, which is also responsible for energy dissipation, cf. Fig 2, give the absolute same maximum load.

Additionally we need to remark, that for small values of $l_c < 0.05$ m the way of fracture changes. This

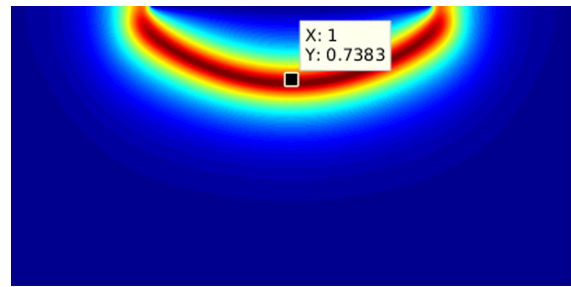


Fig. 8 Position of the crack in the two-dimensional model of the pulled half-space

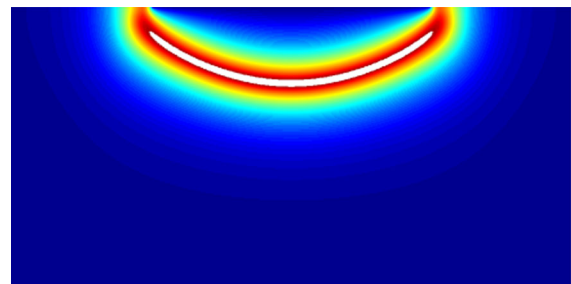


Fig. 9 Crack surface in the two-dimensional model of the pulled half-space, computed with $\mathcal{G}_c = 1$ N/mm and $l_c = 0.1$ m and a mesh of 512×512 elements, $h = 3.9$ mm

effect is induced by the stress singularity at the corner which follows from the linear elastic solution and is captured by a fine discretization. In a fine mesh, with a small diffuse zone l_c , the stress singularities at the corners $y = \pm a$ dominate the overall stress distribution and induce fracture, see Fig. 11. A coarser mesh levels out the (artificial) stress peak and so does a wider diffuse width l_c . In Fig. 12 the load–displacement curves of the two different crack modes can be seen and it also becomes clear the solution is otherwise mesh independent. For the same values of \mathcal{G}_c and l_c the curves lay on top of each other.

6 A conchoidal fracture example

In this section we simulate a three-dimensional bloc of brittle rock material which is loaded in such a way, that it will crack by conchoidal fracture. The model has been suggested to work as a benchmark problem [27] in the framework of our DFG Priority Programm 1748.

The main challenge of conchoidal fracture is that it requires the ability of a numerical method to predict

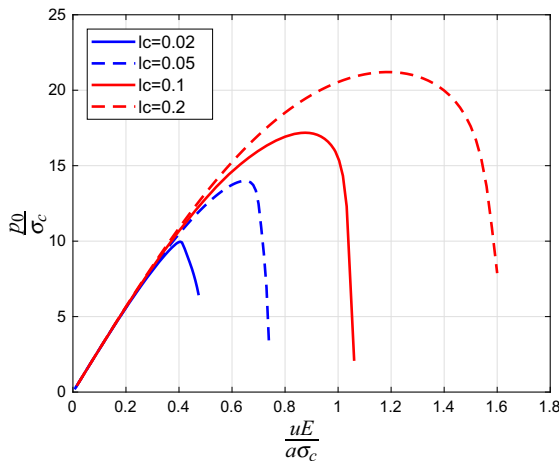


Fig. 10 Load-deflection curves for different length scale parameter l_c referred to the overall mesh size of $h = 0.0078$ m with the characteristic stress $\sigma_c = \sqrt{\mathcal{G}_c E / l_c}$

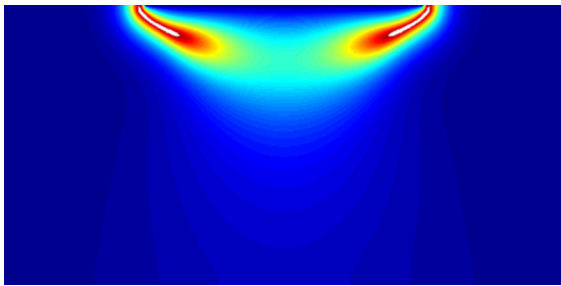


Fig. 11 Crack surface in the two-dimensional model of the pulled half-space, computed with $l_c < 0.05$ m and a mesh of 512×512 elements, $h = 3.9$ mm

crack nucleation and fracture in a brittle material without stress concentration at a notch or at an initial crack.

Often it is induced by an impact, and sometimes one can see the effect of shock waves emanating outwards from the impacted point leaving their mark on the stone as ripples. However, also static loading can induce the typical mussel shell like shape and the faceted surfaces of conchoidal fracture. Thus we employ here a quasistatic, displacement driven loading regime.

We investigate a $4a \times 4a \times 2a$ bloc of stone material subjected to a prescribed displacement on part of its upper boundary, $2a = 1$ m. The geometrical setup of the problem and the boundary conditions are displayed in Fig. 13. On the lower boundary we

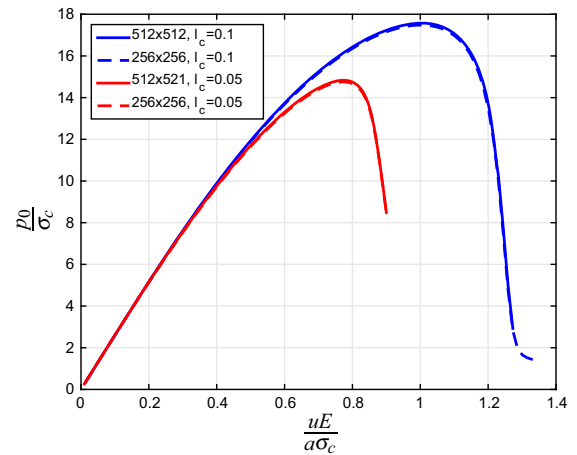


Fig. 12 Load-deflection curves for $l_c = 0.1$ m and $l_c = 0.05$ m, each computed with a mesh of 256×256 elements (dashed lines) and a mesh of 512×512 elements (solid lines)

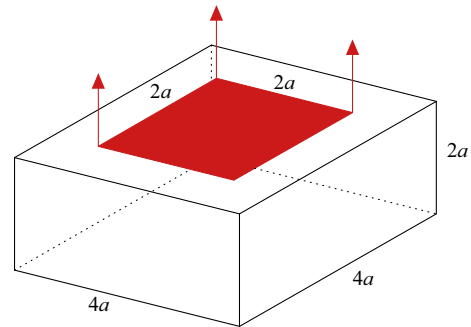


Fig. 13 Geometry and loading of a bloc of brittle rock-like material subjected to tension on the upper exterior surface

prescribe Dirichlet conditions $\mathbf{u} = 0$ and $z = 0$ for the displacements and the crack phase field. The material parameters are chosen as Lamè constant $\lambda = 100,000$ N/mm², shear modulus $\mu = 100,000$ N/mm², and a critical energy release rate of $\mathcal{G}_c = 1$ N/mm.

The finite element mesh requires a certain minimum element size h in order to resolve the geometry with a length scale parameter of $l_c = 0.2$ m. Thus, we discretize the bloc with a structured mesh consisting of 27,000 8-node brick elements. The mesh is *not* refined in the area where the crack is expected to propagate—because we do not want to nudge the simulation in any direction.

The specimen is subject to a displacement-driven deformation by prescribed incremental displacements

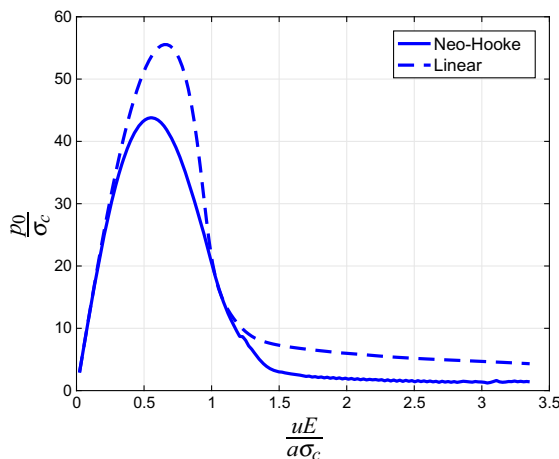


Fig. 14 Force–displacement curve obtained for the linear and non-linear elastic model with the characteristic stress $\sigma_c = \sqrt{\mathcal{G}_c E / l_c}$

of 0.001 mm until crack initiation. The subsequent deformation demands an adjustment of the displacement increments to 0.0001 mm up to the final deformation. The block cracks at a prescribed displacement of about 3 mm, see Fig. 14. The behavior is characterized by a brutal and complete crack growth. In Figs. 15 and 16 the crack evolution at different stages of the deformation is displayed for the linear-elastic model (1) and the non-linear model (16), respectively.

In the linear-elastic as well as in the non-linear elastic model we find crack initiation inside the bloc below the pulled surface. Moreover, both materials show a very similar shape of fracture with the linearized kinematics model being more round. Please note that the characteristic rippled surface of conchoidal fracture can perfectly be observed.

In total the deformation of the bloc is small to moderate. Consequently, the nonlinear Neo–Hookean material model gives results which are very similar to the linear theory. The corresponding load–displacement curves are identical at the beginning but differ in the maximum load of crack initialization, see Fig. 14. Moreover, this example is investigated for different refinement levels for the linear-elastic model. In Fig. 17 the force–displacement curves are presented which differ also in the maximum load of crack initialization. Further studies solver performance are conducted for the linear-elastic model and follow in the next section.

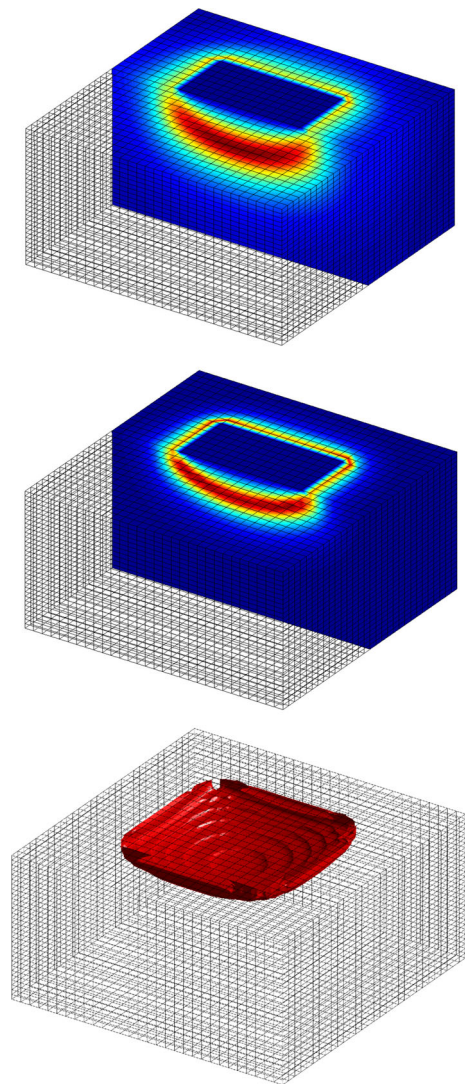


Fig. 15 Region of crack initiation, final state and crack surface in the linear-elastic model computed with a mesh of $30 \times 30 \times 30$ elements

7 Solver benchmark

7.1 Technical specification

We have implemented the multigrid solver used for this simulations in the C++ language as part of our newly developed library UTOPIA, [41]. UTOPIA is an embedded domain specific language (EDSL), designed to make implementations for parallel computing as transparent as possible. UTOPIA enables us to write complex scientific code by using expressions

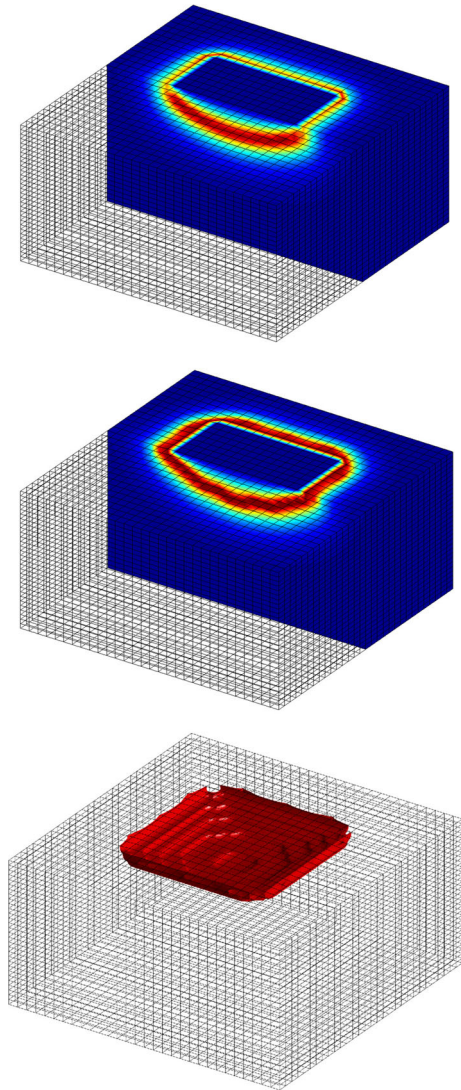


Fig. 16 Region of crack initiation, final state and crack surface in the Neo-Hookean model computed with a mesh of $30 \times 30 \times 30$ elements

similar to the language used in Matlab [16], whereas it hides the complexity of parallelization and machine-specific optimizations in different back-ends. The presented numerical results were obtained by using our back-end for the PETSc library [5].

Our implementation of the multigrid solver employs an LU factorization provided by package MUMPS [4] for the direct solution on level $l = 0$. We used the Gauß-Seidel method for smoothing and performed 3 pre-smoothing and 3 post-smoothing steps on each level $l > 0$. We set $L = 2$ and obtained

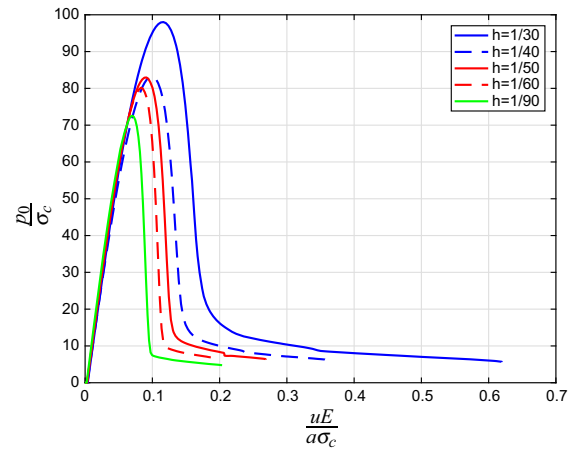


Fig. 17 Force-displacement curve obtained for different refinement levels for the linear-elastic model. Parameter h representing the mesh size was used to discretize the domain with $1/h \times 2/h \times 1/h$ elements. Length scale parameter l_c was chosen as $l_c = 2h$

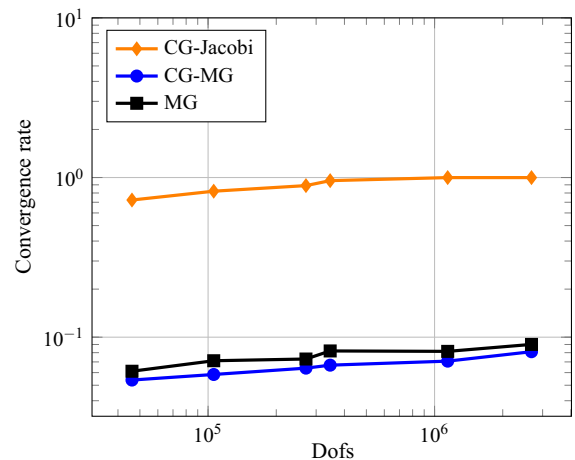


Fig. 18 Average convergence rates for the linear mechanical subproblem

the nested mesh-hierarchy $(\mathcal{T})_{l=0,1,2}$ by means of uniform refinement. Arising nonlinearities are tackled by Newton line-search method with cubic interpolation [26]. For the finite element discretization and assembling we used the MOOSE library [13] together with our extensions.

All tests were performed using the local cluster at the Institute of Computational Science (ICS), Università della Svizzera Italiana, consisting of 24 compute nodes, each equipped with 2 Intel R E5-2650 v3

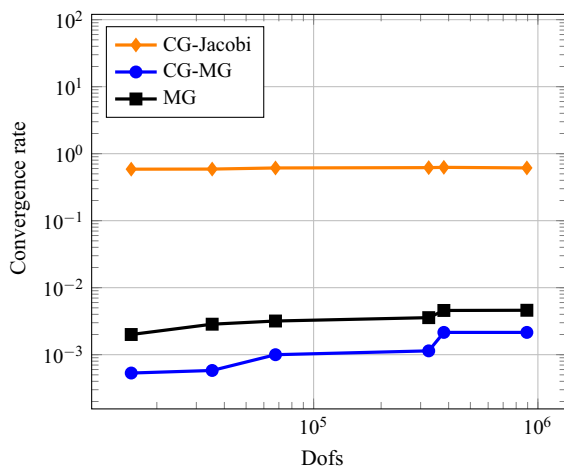


Fig. 19 Average convergence rates for phase field subproblem

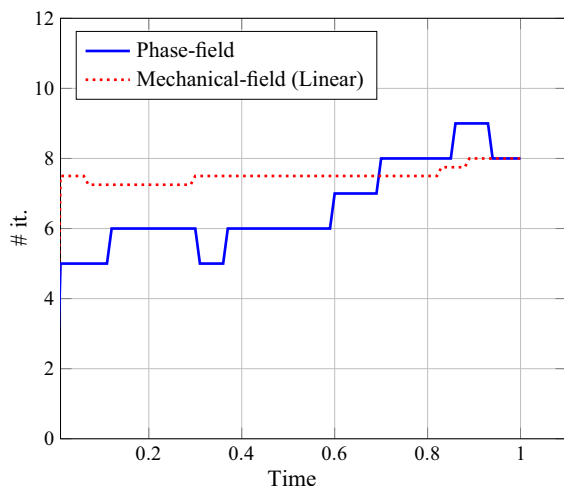


Fig. 20 Average number of CG-MG iterations per time-step over all time-steps. Simulation performed on cube $50 \times 50 \times 25$

processor with a clock-frequency of 2.60GHz. With 10 cores per processors this leads to 20 cores per node. Main memory per node is 64 GB;

7.2 Performance

In this section, we investigate the performance of the multigrid method as a solution method and as a preconditioner inside a preconditioned conjugate gradient method (PCG). Additionally, we perform a comparison with a conjugate gradient method preconditioned by a simple Jacobi step. During all simulations we used as a stopping criterion $\|r\| \leq 10^{-12}$,

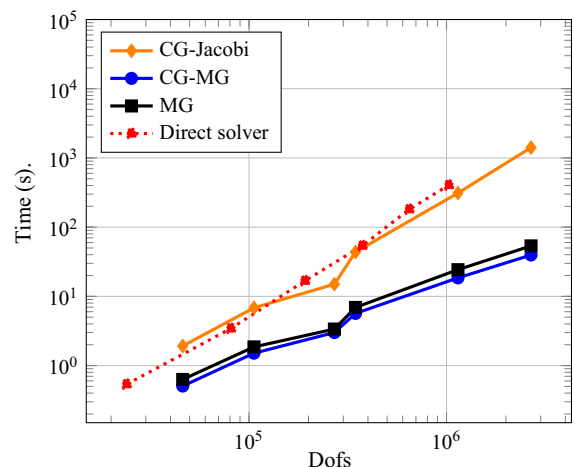


Fig. 21 Average time complexity solution time for one linear solve for the mechanical subproblem. Results obtained without parallelization

where $\|r\|$ is the Euclidian norm of the respective linear residual.

As a first metric, we investigate the estimates

$$\rho = \frac{\|x_{k+1} - x_k\|}{\|x_k - x_{k-1}\|}, \quad (32)$$

for the convergence rates of the iterative solvers. Here, x^k represents the k -th iterate. Figures 18 and 19 depict the average values of ρ , obtained for the mechanical and the phase field subproblems, respectively. We refer to an average convergence rates as to the average over all linear solves over all time-steps.

As expected, the multigrid method shows h -independence property convergence and the number of iterations does not change with an increasing number of degrees of freedom.

Moreover, we investigate how the different solution methods perform during the whole simulation, i.e. their robustness with respect to an enlarged crack area. As we can see from Fig. 20, the number of iterations for the displacement field stays more or less constant during the whole simulation. The number of iterations for the phase field variable increases slightly with growing crack. However, the convergence rate stays even in then most demanding scenario quite low.

We also investigate the efficiency of our solution methods and of their implementation by means of the overall simulation time. For this reason, we monitor the average time in seconds for all linear solves during

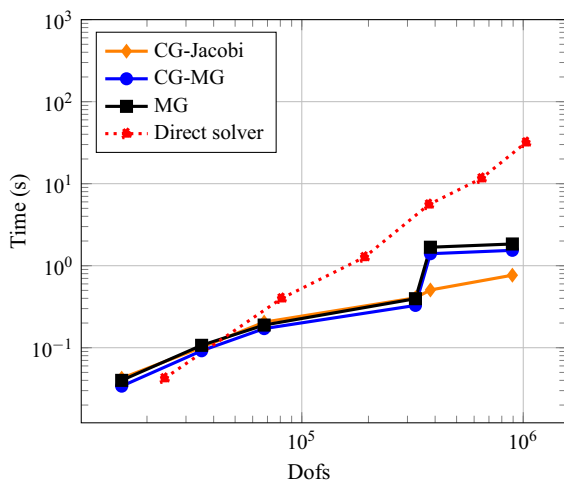


Fig. 22 Average time complexity of one linear solve for phase-field subproblem. Results obtained without parallelization

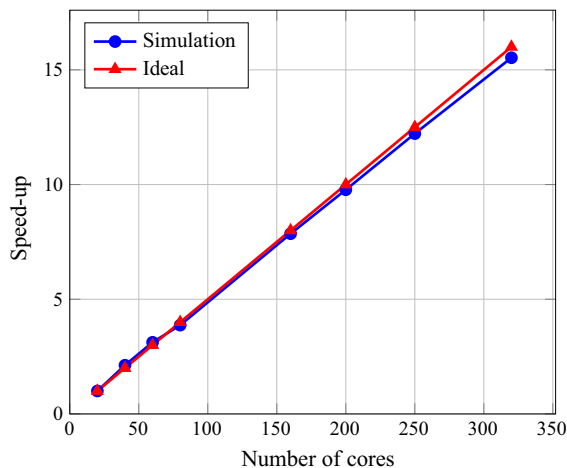


Fig. 23 Strong scaling results for one V-cycle of mechanical subproblem with 1, 142, 778 dofs

the whole simulation. Figures 21 and 22 show a comparison of the average time obtained from different linear solvers for different sizes of the linear systems. Please note, that reported times are based on results obtained on serial machine and do not include any parallelization.

As pointed out above, one of the major advantages of multigrid methods—beyond their optimal complexity—is the fact that they parallelize well. We therefore additionally investigate the strong scalability properties of our UTOPIA implementation of the multigrid method. More precisely, we investigate the

behavior of the method with respect to computational time in order to increase the number of processes but fixed problem size. Figure 23 shows that our implementation gives rise to almost ideally scaling.

8 Conclusions

In this paper the focus is set on conchoidal fracture and the numerical applicability of a phase-field model to identify the location of crack initiation without a pre-crack, a notch or a kerf. Therefore, a suitable benchmark problem in two and three dimensions with regard to the curved breakage, is specified and presented within a series of numerical investigations. The simulations are based on anisotropic splits for both linear and non-linear material models. The main result is that the location of crack initiation heavily depends on the geometry and the length-scale parameter. Thus, the model is very sensitive concerning the choice of length-scale parameter. Furthermore, the multigrid method is demonstrated as solution technique and is combined with the proposed phase-field ansatz. One of the main advantages of this solution technique is the parallelization which leads to a quite low overall simulation time compared with other standard solvers. This paper demonstrates that the phase-field model can properly predict the crack initiation and propagation with an appropriate choice of parameters. Moreover, it is a useful approach to combine the multigrid method with the phase-field ansatz to improve the computational effort concerning the simulation time. In future work this combination will be extended to be applicable with NURBS and with coupling additional fields.

Acknowledgements The authors gratefully acknowledge the support of the Deutsche Forschungsgesellschaft (DFG) under the project “Large-scale simulation of pneumatic and hydraulic fracture with a phase-field approach” as part of the Priority Programme SPP1748 “Reliable Simulation Techniques in Solid Mechanics. Development of Non-standard Discretisation Methods, Mechanical and Mathematical Analysis”.

Funding This study was funded by the German Research Foundation (DFG) under Grant WE2525-4/1.

Compliance with ethical standards

Conflict of interest The authors declare that they have no conflict of interest.

References

1. en.wikipedia.org/wiki/Obsidian/media
2. Abdollahi A, Arias I (2012) Phase-field modeling of crack propagation in piezoelectric and ferroelectric materials with different electromechanical crack conditions. *J Mech Phys Solids* 60(12):2100–2126
3. Ambrosio L, Tortorelli VM (1990) Approximation of functionals depending on jumps by elliptic functionals via Γ -convergence. *Commun Pure Appl Math* 43:999–1036
4. Amestoy PR, Duff IS, L'Excellent J-Y, Koster J (2000) Mumps: a general purpose distributed memory sparse solver. In: *International workshop on applied parallel computing*. Springer, pp 121–130
5. Balay S, Brown J, Buschelman K, Eijkhout V, Gropp W, Kaushik D, Knepley M, McInnes LC, Smith B, Zhang H (2012) PETSc users manual revision 3.3. Computer Science Division, Argonne National Laboratory, Argonne, IL
6. Borden MJ, Verhoosel CV, Scott MA, Hughes TJR, Landis CM (2012) A phase-field description of dynamic brittle fracture. *Comput Methods Appl Mech Eng* 217–220:77–95
7. Borden MJ, Hughes TJR, Landis CM, Verhoosel CV (2014) A higher-order phase-field model for brittle fracture: formulation and analysis within the isogeometric analysis framework. *Comput Methods Appl Mech Eng* 273:100–118
8. Borden MJ, Hughes TJR, Landis CM, Anvari A, Lee IJ (2016) A phase-field formulation for fracture in ductile materials: finite deformation balance law derivation, plastic degradation, and stress triaxiality effects. *Comput Methods Appl Mech Eng* 312:130–166
9. Bourdin B (2007) The variational formulation of brittle fracture: numerical implementation and extensions. In: *Volume 5 of IUTAM symposium on discretization methods for evolving discontinuities*, IUTAM bookseries, chapter 22. Springer, Dordrecht, pp 381–393
10. Bourdin B, Francfort GA, Marigo J-J (2000) Numerical experiments in revisited brittle fracture. *J Mech Phys Solids* 45:797–826
11. Briggs WL, McCormick SF et al (2000) A multigrid tutorial. SIAM, Philadelphia
12. Francfort GA, Marigo J-J (1998) Revisiting brittle fracture as an energy minimization problem. *J Mech Phys Solids* 46:1319–1342
13. Gaston D, Newmann C, Hansen G, Lebrun-Grandie D (2009) MOOSE: a parallel computational framework for coupled systems of nonlinear equations. *Nucl Eng Des* 239:1768–1778
14. Geist GA, Romine CH (1988) Lu factorization algorithms on distributed-memory multiprocessor architectures. *SIAM J Sci Stat Comput* 9(4):639–649
15. Gerasimov T, De Lorenzis L (2016) A line search assisted monolithic approach for phase-field computing of brittle fracture. *Comput Methods Appl Mech Eng*. doi:[10.1016/j.cma.2015.12.017](https://doi.org/10.1016/j.cma.2015.12.017)
16. Guide MU (1998) The mathworks, vol 5. Inc, Natick, p 333
17. Henry H, Levine H (2004) Dynamic instabilities of fracture under biaxial strain using a phase field model. *Phys Rev Lett* 93:105505
18. Hesch C, Gil AJ, Ortigosa R, Dittmann M, Bilgen C, Betsch P, Franke M, Janz A, Weinberg K (2017) A framework for polyconvex large strain phase-field methods to fracture. *Comput Methods Appl Mech Eng* 317:649–683
19. Hesch C, Weinberg K (2014) Thermodynamically consistent algorithms for a finite-deformation phase-field approach to fracture. *Int J Numer Methods Eng* 99:906–924
20. Johnson KL (1987) *Contact mechanics*. Cambridge University Press, Cambridge
21. Karma A, Kessler DA, Levine H (2001) Phase-field model of mode III dynamic fracture. *Phys Rev Lett* 81:045501
22. Kuhn C, Müller R (2010) A continuum phase field model for fracture. *Eng Fract Mech* 77:3625–3634
23. Mariani S, Perego U (2003) Extended finite element method for quasi-brittle fracture. *Int J Numer Methods Eng* 58:103–126
24. Miehe C, Hofacker M, Welschinger F (2010) A phase field model for rate-independent crack propagation: robust algorithmic implementation based on operator splits. *Comput Methods Appl Mech Eng* 199:2765–2778
25. Miehe C, Welschinger F, Hofacker M (2010) Thermodynamically consistent phase-field models of fracture: variational principles and multi-field FE implementations. *Int J Numer Methods Eng* 83(10):1273–1311
26. Nocedal J, Wright SJ (2006) *Numerical optimization*. Springer, New York
27. Müller R (2016) A benchmark problem for phase-field models of fracture. Presentation at the annual meeting of SPP 1748: reliable simulation techniques in solid mechanics. Development of non-standard discretisation methods, mechanical and mathematical analysis, Pavia
28. Ortiz M, Pandolfi A (1999) Finite-deformation irreversible cohesive elements for three-dimensional crack-propagation analysis. *Int J Numer Methods Eng* 44(9):1267–1282
29. Pandolfi A, Ortiz M (2012) An eigenerosion approach to brittle fracture. *Int J Numer Methods Eng* 92:694–714
30. Roe KL, Siegmund T (2003) An irreversible cohesive zone model for interface fatigue crack growth simulation. *Eng Fract Mech* 70(2):209–232
31. Saad Y (2003) *Iterative methods for sparse linear systems*. SIAM, Philadelphia
32. Schenk O, Gärtner K (2004) Solving unsymmetric sparse systems of linear equations with pardiso. *Future Gener Comput Syst* 20(3):475–487
33. Schmidt B, Leyendecker S (2009) Γ -convergence of variational integrators for constraint systems. *J Nonlinear Sci* 19:153–177
34. Sneddon Ian N (1965) The relation between load and penetration in the axisymmetric Boussinesq problem for a punch of arbitrary profile. *Int J Eng Sci* 3:47–57
35. Sukumar N, Srolovitz DJ, Baker TJ, Prevost J-H (2003) Brittle fracture in polycrystalline microstructures with the extended finite element method. *Int J Numer Methods Eng* 56:2015–2037
36. Verhoosel CV, de Borst R (2013) A phase-field model for cohesive fracture. *Int J Numer Methods Eng* 96:43–62
37. Wallner H (1939) Linienstrukturen an Bruchflächen. *Zeitschrift für Physik* 114:368–378
38. Weinberg K, Dally T, Schuss S, Werner M, Bilgen C (2016) Modeling and numerical simulation of crack growth and damage with a phase field approach. *GAMM-Mitt* 39:55–77

39. Weinberg K, Hesch C (2017) A high-order finite deformation phase-field approach to fracture. *Contin Mech Thermodyn* 29:935–945
40. Xu X-P, Needleman A (1994) Numerical simulations of fast crack growth in brittle solids. *J Mech Phys Solids* 42(9):1397–1434
41. Zulian P, Kopaničáková A, Schneider T (2016) Utopia: A c++ embedded domain specific language for scientific computing. <https://bitbucket.org/zulianp/utopia>